Robust Estimation of Metal Target Shape Using Time-Domain Electromagnetic Induction Data

Davorin Ambruš, *Member, IEEE*, Darko Vasić, *Member, IEEE*, and Vedran Bilas, *Senior Member, IEEE*

Abstract—Discriminating metal parts of buried hazardous targets from ordinary metallic clutter is a very difficult and time-consuming task. For that purpose, electromagnetic induction (EMI) sensors composed of multiple transmitter/receiver coils in multiaxis arrangements are commonly used. In this way, data of high fidelity and spatial diversity are obtained so that the target can be characterized in terms of its geometric and electromagnetic properties. However, this often increases sensor size and reduces its portability, which is a problem for humanitarian demining applications, where compact, robust, and lightweight sensors are needed. If such sensors are to be used for target characterization, robust estimation algorithms are required, capable of coping with limited spatial information content and uncertainties related to sensor positioning and its coil geometry model. In this paper, we present a robust concept for estimating the general shape of magnetic metal targets using time-domain EMI sensors with single-axis coil geometries. We introduce the signature matrix, a parameter derived from time-dependent eigenvalues of the target's magnetic polarizability tensor, and use it for shape estimation. The proposed method was evaluated both through simulations and experiments, using two different sensor platforms (laboratory-based experimental sensor platform and a commercial metal detector mounted on a mobile robot). The obtained results clearly indicate that the target shape can be estimated from sensor data of limited spatial diversity and under the uncertainties of sensor positioning and coil geometry.

Index Terms—Electromagnetic induction (EMI), electromagnetic modeling, magnetic polarizability tensor, target shape estimation.

I. INTRODUCTION

DETECTION of buried landmines is a crucial and most dangerous part of humanitarian demining (HD) since it normally involves human deminers performing hazardous tasks in the field [1], [2]. At present, primary tools for close-in detection of landmines are handheld metal detectors (MDs) [2]–[4] and mechanical prodders [4], [5]. Conventional MDs used in HD operate on basic principles of electromagnetic induction (EMI), featuring high sensitivity to extremely low quantities of metal, such as those found in low-metal content landmines. On the other hand, enormous false alarm rates (up to 1000 alarms/mine) are introduced due to detectors' inability to discriminate between metal parts of a mine and innocuous metallic clutter [2], [3]. In order to reduce the number of false alarms and obtain faster, safer, and cheaper mine clearance, there has been a strong motivation to develop novel EMI sensors capable of target discrimination and classification.

EMI sensors used for metal target detection operate in low-frequency magnetoquasistatic regime (mostly between 10 Hz and 100 kHz), which severely limits the possibility of using subsurface imaging as a target discrimination tool, due to its very low spatial resolution. Recently, novel approaches to EMI imaging have emerged, relying either on next-generation sensors for unexploded ordnance (UXO) detection and advanced target models [6] or on the application of a mobile sensor network for creating an image of a magnetic anomaly around a target [7]. However, a much more practical and robust alternative to EMI imaging, particularly for low metal content targets, is to search for intrinsic target EMI signatures that strongly correlate with target geometry, e.g., its shape [8].

Different classification approaches based on metal target signatures have been investigated, including deterministic and stochastic techniques, with a detailed overview given in [9]. Although some of these methods use nonphenomenological features of EMI response [10], most of them rely on analytical models utilizing the magnetic dipole approximation to first characterize the target in terms of its intrinsic geometric and electromagnetic properties [11]–[15] and then use parameters of such models to feed the target classification algorithms [9]. Small targets, such as low metal content landmines, may be well characterized by models relying on a single induced magnetic dipole, represented by its magnetic polarizability tensor [12], [16], [17]. Recently, such a modeling approach has been successfully applied in security applications [18] and food contamination monitoring [19].

When it comes to parameter estimation of a dipole model, sensor configurations composed of multiple transmitter (TX) and receiver coils (RXs) in multiaxis arrangements are preferred so that the target is interrogated with magnetic fields of different orientations from a single sensor location [9], [20], [21]. In this way, data of high fidelity and spatial diversity can be obtained, but at the expense of increased sensor size and reduced portability [8]. This is a problem for HD applications, where compact, robust, and lightweight sensors are needed. Such sensors normally employ a single TX and one or more single-axis receivers.

Single-transmitter sensors need to acquire data over multiple sensor positions and orientations in order to subject the target to three orthogonal components of the primary magnetic field

This article has been accepted for inclusion in a future issue of this journal. Content is final as presented, with the exception of pagination.

2   IEEE TRANSACTIONS ON INSTRUMENTATION AND MEASUREMENT

and capture the corresponding target responses so that the target could be characterized unambiguously. The downside is that target parameter estimation gets significantly affected by the uncertainties in sensor positioning [9], [22], [23]. For handheld sensors, a separate system to track the relative pose of the search head in real time needs to be provided. Different solutions have been proposed for that purpose, such as those based on optical correlation sensors [24], ultrasonic triangulation [25], magnetic beacons [26], and special metal markers combined with inertial sensors [27].

One of the emerging application fields in HD is the use of robots equipped with landmine detection sensors as mobile scanning platforms [28]. The use of robot manipulators with two or more degrees of freedom and the precise sensor pose control mitigates the issue of sensor positioning uncertainties normally encountered in handheld sensors. However, since the characterization and localization of targets normally takes place in a stationary and not in a robot-referenced coordinate system, robots need to be equipped with sensor systems providing advanced geolocation capabilities [29], [30]. Recent studies in that field focus mainly on multimodality sensing and data fusion, primarily for MDs and ground penetrating radars [31]. Experiments involving commercial off-the-shelf MDs with robotic manipulators were also reported, dealing with simple target depth estimation [32], or a coarse target discrimination based on a signal matching approach [33], [34].

In this paper, we propose a concept for shape estimation of a magnetic metal target, modeled as an induced magnetic dipole, using time-domain (TD) EMI sensors with single-axis coils. Motivated by the current state of the art in landmine detection technology, our concept is mainly targeted toward robotic applications in HD, although it can be applied to any TD metal detection system if certain conditions are met. In an envisioned scenario, a robot would first detect a target, then perform the spatial mapping of limited coverage and duration, and finally estimate the target's shape and position from acquired data irrespective of its orientation. It is important to note that the concept based on a dipole model cannot provide information on the exact outer shape of a target, but rather a single parameter strongly related to the target's 3-D aspect ratio. However, such information could be of viable help in discriminating the metal parts of hazardous targets (which are mostly axisymmetric) from irregularly shaped clutter items, such as ordnance fragments or metal debris. A detailed study on shape-based UXO/clutter discrimination is given in [35].

There are two major concerns with the given scenario. The first one is related to the limited spatial diversity of data, which could hinder the invertibility of dipole model parameters. The second concern is that the sensor uncertainties could make the estimated parameters unreliable for target classification. In this paper, we analyze two major sources of uncertainties: 1) sensor positioning and 2) the coil geometry model. The novelty of our approach is that it tackles both these concerns using temporal information stored in the target's principal magnetic polarizabilities rather than their magnitudes. This is a key feature that boosts the robustness of our estimation algorithm.
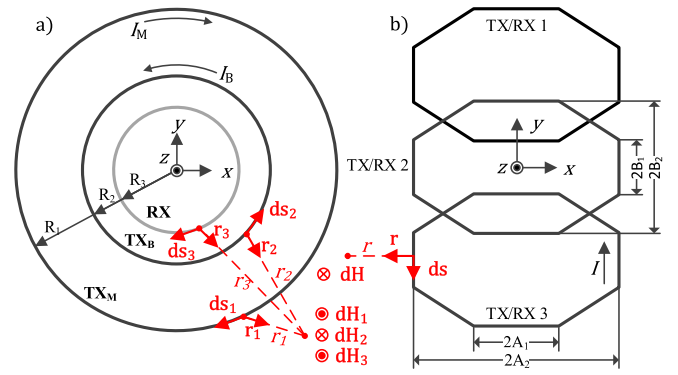

Fig. 1. Models of analyzed sensor coil configurations. (a) Circular coils of the experimental sensor platform. (b) Octagonal coils modeling the Vallon VMP3 sensor. Magnetic fields of current loops are calculated using the Biot–Savart law.

This paper is organized as follows. In Section II, we introduce an analytical forward model describing the basic sensor/target properties and the algorithm for the estimation of dipole model parameters. In Section III, we describe the methodology for target shape estimation. In Section IV, we evaluate its performance under different uncertainties using a synthetic data set and two different sensor configurations. In Sections V and VI, we present the experimental setup and show the results obtained using the experimental sensor platform and the commercial robot-based MD platform, respectively. Conclusions are drawn in Section VII.

II. TARGET CHARACTERIZATION USING THE DIPOLE MODEL

A. Forward Modeling

We derive a forward model that describes the TD EMI response of a dipole target illuminated by the sensor magnetic field from an arbitrary pose above the target. In the first step, we develop the sensor coil geometry model. Two different sensor coil configurations are analyzed (Fig. 1).

The first sensor comprises three coaxial circular coils: two transmitter coils (the main coil TX_M and the bucking coil TX_B) and a single RX [Fig. 1(a)]. The coils are part of an experimental sensor platform, originally developed for frequency-domain operation, where the bucking coil is used to suppress the primary magnetic field within the receiver [36]. In this paper, we use the same coil configuration for TD operation and model the real finite-length coils with ideal circular current loops. The properties of the coils are set in their geometry vector $\mathbf{G}_v = [R_1, R_2, R_3]$ [Fig. 1(a)].

The second sensor that we analyze is a commercial TD MD with three identical TX/RX coils (Vallon, VMP3). For this sensor, we use a simplified model based on octagonal current loops, due to their close resemblance to the shape of the actual coils [Fig. 1(b)]. Another benefit of the octagonal coil model is that its shape can be easily adjusted by varying its four-parameter geometry vector $\mathbf{G}_v = [A_1, A_2, B_1, B_2]$. In this way, it can be adapted to suit different detectors whose search coil shapes closely resemble to an octagon or an oval body with flat ends. Such coil designs are often found in TD MDs used in HD [37], [38].

Neglecting the effects of soil (i.e., assuming the soil with neutral or moderate effects on MDs according to the CWA 14747-2 standard [39]), the magnetic field of any current loop $\mathbf{H}_p$, normalized with respect to the excitation current, can be calculated at any point in space via the Biot–Savart law

$$\mathbf{H}_p = \frac{1}{4\pi} \oint_{\text{coil}} \frac{d\mathbf{s} \times \hat{\mathbf{r}}}{|\mathbf{r}|^2}. \tag{1}$$

Assuming the sensor is mounted on a 2-DoF robotic arm (or manually swept in a similarly controlled manner), its spatial orientation can be described by the two Euler angles: 1) yaw (rotation around the sensor's z-axis, ψ) and 2) pitch (rotation around the sensor's y-axis, θ). The resulting primary magnetic field vector $\mathbf{H}_p$ (observed at the target location $\mathbf{r}_{\text{target}}$) is obtained by transforming the target coordinates (relative to the sensor center position $\mathbf{r}_{\text{sensor}}$) from the stationary reference frame (RF) to the moving sensor frame (SF) (2), calculating the x-, y-, and z-components of a magnetic field in the SF, and then transforming them back to the RF (3). $\mathbf{R}$ is a rotation matrix based on the yaw–pitch–roll rotation formalism (4)

$$\mathbf{r}_{\text{SF}} = \mathbf{R} \cdot (\mathbf{r}_{\text{sensor}} - \mathbf{r}_{\text{target}}) \tag{2}$$

$$\mathbf{H}_p = \mathbf{H}_{p\_\text{RF}} = \mathbf{R}^{\mathbf{T}} \cdot \mathbf{H}_{p\_\text{SF}}(\mathbf{r}_{\text{SF}}) \tag{3}$$

$$\mathbf{R} = \begin{bmatrix} \cos\theta\cos\psi & \cos\theta\sin\psi & -\sin\theta \\ -\sin\psi & \cos\psi & 0 \\ \sin\theta\cos\psi & \sin\theta\sin\psi & \cos\theta \end{bmatrix}. \tag{4}$$

For a sensor with colocated transmitter (TX) and receiver (RX) coils, the induced voltage u_{ind} may be described by (5) using the reciprocity principle [15]. $\mathbf{H}_{p\_\text{TX}}$ is a normalized magnetic field of the TX coil, $\mathbf{H}_{p\_\text{RX}}$ is a normalized magnetic field that would be generated if the RX coil were used as a transmitter, $\mathbf{M}$ is a time-dependent magnetic polarizability tensor (3×3 symmetric matrix containing intrinsic target information), and k is a calibration constant dependent on the excitation current and coil design

$$u_{\text{ind}} = k \cdot \mathbf{H}_{p\_\text{RX}}^{\mathbf{T}}(\mathbf{r}_{\text{target}}) \cdot \mathbf{M}(t) \cdot \mathbf{H}_{p\_\text{TX}}(\mathbf{r}_{\text{target}}). \tag{5}$$

In (5), we assumed an ideal step waveform of the sensor excitation current, which means that TD representation of the primary magnetic field is a Dirac function, whose amplitude is proportional to the excitation current shortly before its switch off. Also, we assume that the elements of $\mathbf{M}$ already incorporate a time derivative, since u_{ind} is also proportional to a time derivative of the measured field [13]. For a TD sensor with a single TX/RX coil [i.e., monocoil sensor, Fig. 1(b)], $\mathbf{H}_{p\_\text{TX}}$ and $\mathbf{H}_{p\_\text{RX}}$ are the same ($\mathbf{H}_p$)

$$u_{\text{ind}} = k \cdot \begin{bmatrix} H_{p\_x} \\ H_{p\_y} \\ H_{p\_z} \end{bmatrix}^T \cdot \begin{bmatrix} m_{11}(t) & m_{12}(t) & m_{13}(t) \\ m_{12}(t) & m_{22}(t) & m_{23}(t) \\ m_{31}(t) & m_{23}(t) & m_{33}(t) \end{bmatrix} \cdot \begin{bmatrix} H_{p\_x} \\ H_{p\_y} \\ H_{p\_z} \end{bmatrix}. \tag{6}$$

The monocoil sensor response (6) can be further rewritten in a vector form (7), where $\mathbf{H}_x$, $\mathbf{H}_y$, and $\mathbf{H}_z$ represent $m \times 1$ size vectors containing x-, y-, and z-components of $\mathbf{H}_p$, respectively, generated at $\mathbf{r}_{\text{target}}$ from m different sensor poses,

TABLE I

ALGORITHM FOR THE ESTIMATION OF THE MAGNETIC POLARIZABILITY VECTOR $\mathbf{M}_v$ AND THE TARGET LOCATION $\mathbf{r}_{\text{target}}$

Initial guess for the target location, $\mathbf{r}_{\text{target\_new}} = \text{index}(\max(\mathbf{u}_{\text{ind}}(\mathbf{r}_{\text{sensor}})))$
Initial guess for the magnetic polarizabilities vector, $\mathbf{M}_{v\_\text{new}} = [1\ 1\ 1\ 1\ 1\ 1]$;
While ($|\mathbf{M}_{v\_\text{new}} - \mathbf{M}_{v\_\text{old}}| > \varepsilon_{\mathbf{M}_v}$ and $|\mathbf{r}_{\text{target\_new}} - \mathbf{r}_{\text{target\_old}}| > \varepsilon_{\mathbf{r}_{\text{target}}}$)
$\quad \mathbf{r}_{\text{target\_old}} \leftarrow \mathbf{r}_{\text{target\_new}}$;
$\quad \mathbf{M}_{v\_\text{old}} \leftarrow \mathbf{M}_{v\_\text{new}}$;
$\quad$ (1) Estimate magnetic polarizabilities vector $\mathbf{M}_v$
$\qquad$ Find solution to:
$\qquad\qquad \mathbf{M}_v = \mathbf{H}_{xyz}^{-1}(\mathbf{r}_{\text{target\_old}}) \cdot \mathbf{u}_{\text{ind}}$
$\quad \mathbf{M}_{v\_\text{new}} \leftarrow \mathbf{M}_v$;
$\quad$ (2) Estimate target location $\mathbf{r}_{\text{target}}$
$\qquad$ Find $\mathbf{r}_{\text{target}}$ that is a solution to:
$\qquad\qquad \arg\min \left(\|\mathbf{u}_{\text{ind}}(\mathbf{M}_{v\_\text{new}}) - f_{\text{FWD}}(\mathbf{r}_{\text{target}})\|^2 \right)$
$\quad \mathbf{r}_{\text{target\_new}} \leftarrow \mathbf{r}_{\text{target}}$;
End

and $\mathbf{u}_{\text{ind}}$ is an $m \times 1$ vector of measured voltages

$$\mathbf{u}_{\text{ind}} = \begin{bmatrix} \mathbf{H}_x \circ \mathbf{H}_x \\ \mathbf{H}_x \circ \mathbf{H}_y \\ \mathbf{H}_x \circ \mathbf{H}_z \\ \mathbf{H}_y \circ \mathbf{H}_y \\ \mathbf{H}_y \circ \mathbf{H}_z \\ \mathbf{H}_z \circ \mathbf{H}_z \end{bmatrix}^T \cdot \begin{bmatrix} m_{11} \\ m_{12} \\ m_{13} \\ m_{22} \\ m_{23} \\ m_{33} \end{bmatrix} \cdot k = \mathbf{H}_{xyz} \cdot \mathbf{M}_v \cdot k. \tag{7}$$

For a multicoil sensor [Fig. 1(a)], it can be shown that its response is given by

$$\mathbf{u}_{\text{ind}} = \begin{bmatrix} \mathbf{H}_{x\_\text{TX}} \circ \mathbf{H}_{x\_\text{RX}} \\ \mathbf{H}_{x\_\text{TX}} \circ \mathbf{H}_{y\_\text{RX}} + \mathbf{H}_{y\_\text{TX}} \circ \mathbf{H}_{x\_\text{RX}} \\ \mathbf{H}_{x\_\text{TX}} \circ \mathbf{H}_{z\_\text{RX}} + \mathbf{H}_{z\_\text{TX}} \circ \mathbf{H}_{x\_\text{RX}} \\ \mathbf{H}_{y\_\text{TX}} \circ \mathbf{H}_{y\_\text{RX}} \\ \mathbf{H}_{y\_\text{TX}} \circ \mathbf{H}_{z\_\text{RX}} + \mathbf{H}_{z\_\text{TX}} \circ \mathbf{H}_{y\_\text{RX}} \\ \mathbf{H}_{z\_\text{TX}} \circ \mathbf{H}_{z\_\text{RX}} \end{bmatrix}^T \cdot \begin{bmatrix} m_{11} \\ m_{12} \\ m_{13} \\ m_{22} \\ m_{23} \\ m_{33} \end{bmatrix} \cdot k. \tag{8}$$

In general, the voltage induced in a sensor coil with a known geometry vector $\mathbf{G}_v$, scaling constant k, and a known pose ($\mathbf{r}_{\text{sensor}}$, ψ, θ) is a nonlinear function of the target position $\mathbf{r}_{\text{target}}$ and a linear function of the magnetic polarizability vector $\mathbf{M}_v$ (9). Parameters $\mathbf{G}_v$ and k are obtained through sensor calibration (see Section VI-D for more details)

$$\mathbf{u}_{\text{ind}}(\mathbf{r}_{\text{sensor}}, \theta, \psi, \mathbf{G}_v, k) = f_{\text{FWD}}(\mathbf{r}_{\text{target}}, \mathbf{M}_v). \tag{9}$$

B. Inversion of Dipole Model Parameters

Estimation of $\mathbf{r}_{\text{target}}$ and $\mathbf{M}_v$ from $\mathbf{u}_{\text{ind}}$ is realized by an iterative algorithm that sequentially calculates the linear and nonlinear least-squares solutions for $\mathbf{M}_v$ and $\mathbf{r}_{\text{target}}$, respectively, until the preset error limits are reached (Table I). The algorithm starts with an initial guess for $\mathbf{r}_{\text{target}}$ by finding the sensor position that corresponds to the maximal value of the induced voltage within the data set.

The nonlinear part of the optimization algorithm is based on the Levenberg–Marquardt method and is realized in MATLAB using a built-in solver function *lsqnonlin*. Different optimization algorithms based on the trust region method have also been tried, with almost identical results.

For a general case of a sensor that provides measured data acquired at N time instances (i.e., gates) along the pulse decay curve, the forward function can be formulated as (10). From there, a computationally efficient inversion algorithm can be realized so that polarizability vectors $\mathbf{M}_v$ corresponding to different time gates (TGs) can be estimated simultaneously

$$
\begin{bmatrix} \mathbf{u}_{\text{ind}}(t_1) \\ \mathbf{u}_{\text{ind}}(t_2) \\ \vdots \\ \mathbf{u}_{\text{ind}}(t_N) \end{bmatrix} = \begin{bmatrix} \mathbf{H}_{xyz} & \mathbf{0}_{m,6} & \mathbf{0}_{m,6} \\ \mathbf{0}_{m,6} & \mathbf{H}_{xyz} & \mathbf{0}_{m,6} \\ \vdots & \vdots & \vdots \\ \mathbf{0}_{m,6} & \mathbf{0}_{m,6} & \mathbf{H}_{xyz} \end{bmatrix} \cdot \begin{bmatrix} \mathbf{M}_v(t_1) \\ \mathbf{M}_v(t_2) \\ \vdots \\ \mathbf{M}_v(t_N) \end{bmatrix} \cdot k. \quad (10)
$$

III. TARGET SHAPE ESTIMATION

In general, the magnetic polarizability tensor $\mathbf{M}$ makes a good basis for development of metal target classifiers, since it contains unbiased information that is specific to the target under inspection. The tensor can be decomposed into its eigenvalues λ by means of a diagonalization matrix $\mathbf{D}$

$$
\mathbf{M} = \mathbf{D}^T \begin{bmatrix} \lambda_{11}(t) & 0 & 0 \\ 0 & \lambda_{22}(t) & 0 \\ 0 & 0 & \lambda_{33}(t) \end{bmatrix} \mathbf{D}. \quad (11)
$$

These eigenvalues may be interpreted as coefficients that transform components of the primary magnetic field at the target center to the induced magnetic dipole moment oriented along the corresponding principal axes (PAs) of a target (λ_{11}, λ_{22}, and λ_{33} relate to target's PA x, y, and z, respectively). Information on target's size, shape, and material properties can be inferred from λ, while the columns of $\mathbf{D}$ (i.e., the tensor eigenvectors) contain the spatial orientation of target's PA [13], [23].

A. Signature Matrix

The concept of using the magnitudes of tensor eigenvalues λ_{ii} or their mutual ratios $\lambda_{ii}/\lambda_{jj}$ for target shape estimation is not new. Some early studies from that field suggested that it could be successfully applied to a range of metal targets, but with low reliability when used with standard single-axis EMI sensors [40]. In this paper, we employ and further elaborate a different concept introduced in [41] that relies on temporal information stored in λ_{ii} for robust shape-based classification.

We use sensor data corresponding to three different TGs, invert for $\lambda_{\text{PA}}(t_{\text{TG}})$, where PA $= \{11, 22, 33\}$ and TG $= \{1, 2, 3\}$, and then calculate the signature matrix $\mathbf{S}$ (12). We first calculate the ratios of eigenvalues that relate to the same PA but are inverted from data acquired at different TGs. In this way, temporal information is utilized for obtaining a simple target signature for each PA separately (s_{11}, s_{22}, s_{33}). This is a key feature that provides estimation robustness, as will be shown later on. In the next step, ratios of these signatures belonging to different PA are calculated for each pair of PA

$$
\mathbf{S} = \begin{bmatrix} \dfrac{\lambda_{11}(t_1)/\lambda_{11}(t_2)}{\lambda_{22}(t_1)/\lambda_{22}(t_2)} & \dfrac{\lambda_{11}(t_1)/\lambda_{11}(t_2)}{\lambda_{33}(t_1)/\lambda_{33}(t_2)} & \dfrac{\lambda_{22}(t_1)/\lambda_{22}(t_2)}{\lambda_{33}(t_1)/\lambda_{33}(t_2)} \\[2mm] \dfrac{\lambda_{11}(t_1)/\lambda_{11}(t_3)}{\lambda_{22}(t_1)/\lambda_{22}(t_3)} & \dfrac{\lambda_{11}(t_1)/\lambda_{11}(t_3)}{\lambda_{33}(t_1)/\lambda_{33}(t_3)} & \dfrac{\lambda_{22}(t_1)/\lambda_{22}(t_3)}{\lambda_{33}(t_1)/\lambda_{33}(t_3)} \\[2mm] \dfrac{\lambda_{11}(t_2)/\lambda_{11}(t_3)}{\lambda_{22}(t_2)/\lambda_{22}(t_3)} & \dfrac{\lambda_{11}(t_2)/\lambda_{11}(t_3)}{\lambda_{33}(t_2)/\lambda_{33}(t_3)} & \dfrac{\lambda_{22}(t_2)/\lambda_{11}(t_3)}{\lambda_{33}(t_2)/\lambda_{33}(t_3)} \end{bmatrix}.
$$

$$(12)$$

B. Relating Signature Matrix to Target Shape

In order to interpret the physical background of a signature matrix and explain its relationship to target shape estimation, we start from the well-known empirical model that describes the intrinsic response of a metal target in one of its PA in terms of its magnitude and shape of its time decay curve (13) [13]. Taking the ratio of target responses from the same PA at two different TGs, we obtain the target signature (14)

$$
\lambda_{11}(t_1) = k_{11}(t_1 + \alpha_{11})^{-\beta_{11}} \exp\left(\frac{-t_1}{\gamma_{11}}\right) \quad (13)
$$

$$
s_{11} = \frac{\lambda_{11}(t_1)}{\lambda_{11}(t_2)} = \frac{(t_1 + \alpha_{11})^{-\beta_{11}}}{(t_2 + \alpha_{11})^{-\beta_{11}}} \exp\left[\frac{-1}{\gamma_{11}}(t_1 - t_2)\right]. \quad (14)
$$

From (14), we observe that the target signature is now scaled with respect to its magnitude and determined only by α, β, and γ, which control the duration and shape of three characteristic stages of the decay curve: 1) early time; 2) intermediate time; and 3) late time stage, respectively. Since most MDs operate in the intermediate time stage, where the response is governed by $t^{-\beta}$, taking the natural logarithm of (14) and dividing by the signature of the other PA, we obtain

$$
\alpha_{11} \ll t_1, t_2 \wedge \gamma_{11}, \gamma_{22} \gg t_1, \quad t_2 \xrightarrow{\text{yields}} \frac{\ln(s_{11})}{\ln(s_{22})} \approx \frac{\beta_{11}}{\beta_{22}}. \quad (15)
$$

The ratio of time decay rates β_{ii}/β_{jj} is a property strongly related to the target shape [13]. This effect is, however, observed for magnetic targets only [42]. In general, a magnetic target will exhibit a steeper response decay for a given PA (higher β) when the primary field is aligned perpendicularly to it. In other words, the elements of the signature matrix may be regarded as magnetic aspect ratios inversely proportional to target's corresponding geometrical aspect ratios. For instance, the signature matrix of a magnetic sphere would ideally be equal to the identity matrix, whereas elongated magnetic objects with their dominant PA in the x-direction (s_{11}) would cause all the matrix elements with s_{11} in the denominator to be smaller than 1 and all the other elements to be greater than 1.

C. Target Signature Estimation Under Uncertainties

For the purpose of our analysis, we now consider a magnetic dipole with nonzero elements on the diagonal of its magnetic polarizability tensor, i.e., a target whose PA are parallel to the x-, y-, and z-axes of the coordinate system (m_{ii} equal to λ_{ii}). Further, if we observe a special case in which the target has only one dominant polarizability component (magnetic rod and nonmagnetic disk), or two or three dominant polarizability components of equal magnitudes (symmetric magnetic disk
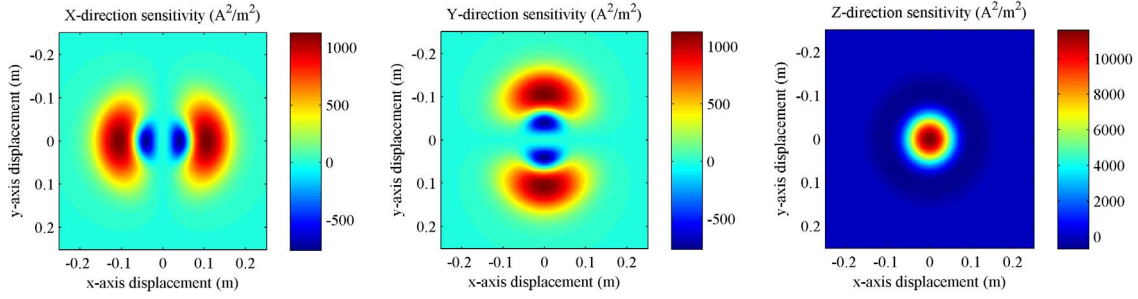
This article has been accepted for inclusion in a future issue of this journal. Content is final as presented, with the exception of pagination.

AMBRUŠ *et al.*: ROBUST ESTIMATION OF METAL TARGET SHAPE USING TD EMI DATA   5

Fig. 2.   Spatial distribution of the sensitivity in the *x*-, *y*-, and *z*-directions for the circular multicoil sensor, whose *xy* plane is 5 cm below the sensor.
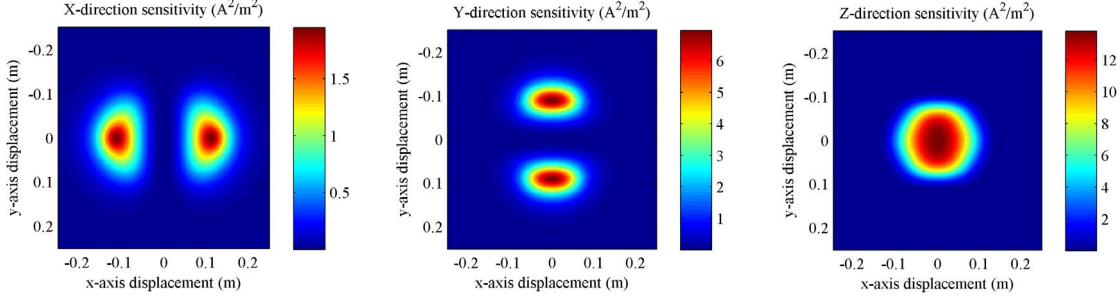

Fig. 3.   Spatial distribution of the sensitivity in the *x*-, *y*-, and *z*-directions for the octagonal monocoil sensor, whose *xy* plane is 5 cm below the sensor.

and metallic sphere), the ratio of polarizabilities obtained at two different TG is given by (16), where $\mathbf{h}_{xyz}^{\dagger}$ is a Moore–Penrose pseudoinverse vector

$$s_{ii} = \frac{m_{ii}(t_1)}{m_{ii}(t_2)} = \frac{\mathbf{h}_{xyz}^{\dagger}(\mathbf{r}_{\text{sensor}}, \mathbf{G}_v) \cdot \mathbf{u}_{\text{ind}}(t_1)}{\mathbf{h}_{xyz}^{\dagger}(\mathbf{r}_{\text{sensor}}, \mathbf{G}_v) \cdot \mathbf{u}_{\text{ind}}(t_2)}. \qquad (16)$$

From (16), it is clear that the uncertainties related to sensor positioning $\mathbf{r}_{\text{sensor}}$, sensor coil geometry $\mathbf{G}_v$, and induced voltage measurement $\mathbf{u}_{\text{ind}}$ tend to cancel mutually. This feature increases the overall robustness of the estimation algorithm. It also loosens the requirements for the initial calibration of the sensor geometry model. Intuitively, a similar assumption can also be made for targets with different combinations of eigenvalues and PA orientations.

IV. VALIDATION ON A SYNTHETIC DATA SET

In order to validate the above assumptions, we tested the algorithm for the estimation of target principal polarizabilities m_{ii} and principal signatures s_{ii} using synthetic data with different sources of uncertainties. However, prior to the actual simulation, basic criteria for the selection of the scanning pattern need to be established. This is an important step since it determines the limits of quantity and spatial diversity of sensor data needed for target shape estimation.

A. Scanning Pattern Selection

From (7) and (8), it can be observed that the matrix $\mathbf{H}_{xyz}$ contains the sensor sensitivities to each of the six target's principal polarizabilities m_{ii}. If we again assume a normal target orientation (i.e., its PA parallel to the *x*-, *y*-, and *z*-axes of the coordinate system), then for each target position, the corresponding sensor sensitivities in the *x*-, *y*-, and *z*-directions can be computed. The sensitivity distribution maps for the circular multicoil sensor with a geometry vector

$\mathbf{G}_v = [15 \text{ cm } 6 \text{ cm } 4 \text{ cm}]$ [Fig. 1(a)] and the octagonal monocoil sensor with a $\mathbf{G}_v = [12 \text{ cm } 6 \text{ cm } 9 \text{ cm } 6 \text{ cm}]$ [Fig. 1(b)] are given in Figs. 2 and 3, respectively. The maps are calculated in the *x y* plane located 5 cm below each sensor. Magnetomotive force [MMF, related to the scaling constant k in (7) and (8)] was set at 12, 4, and 200 AT for TX$_M$, TX$_B$, and RX circular coils, respectively, in order to account for the actual sensor parameters. For the octagonal coil, MMF was set at 1 AT. Note that due to different scaling, absolute sensitivities are not to be compared between the two sensors.

From the given sensitivity distributions, it can be observed that once the target is detected and approximately located, the scanning pattern of the sensor coils relative to the target should preferably include the areas where all of the three sensitivities are the highest. If insufficient amounts of data are acquired from these areas during the whole scan, the target shape estimates might become ambiguous due to ill conditioning of the sensitivity matrix. It is also evident from Figs. 2 and 3 that *z*-direction sensitivities dominate over *x*- and *y*-directions sensitivities, as expected for sensors with single-axis coils.

B. Simulations and Results

Basic specifications of the simulation tests performed for the two analyzed sensor configurations are given in Table II. Six tests with various levels of uncertainties attributed to measurement and sensor/target positioning (1–4), as well as coil geometry (5 and 6) were performed. The objective was to find out how these uncertainties propagate to the estimated polarizabilities m_{ii} and target signatures s_{ii} in a scenario of interest. In all tests, measurement and sensor/target position data were corrupted with Gaussian noise of different SNRs. For each test, 100 experiments were simulated to obtain the mean value and standard deviation of estimated parameters.

In the simulations with the circular coil sensor, a generic magnetic dipole with $\mathbf{M}_v(t_1) = [2\ 4\ 6]$ and $\mathbf{M}_v(t_2) = [1\ 2\ 3]$

This article has been accepted for inclusion in a future issue of this journal. Content is final as presented, with the exception of pagination.

6   IEEE TRANSACTIONS ON INSTRUMENTATION AND MEASUREMENT
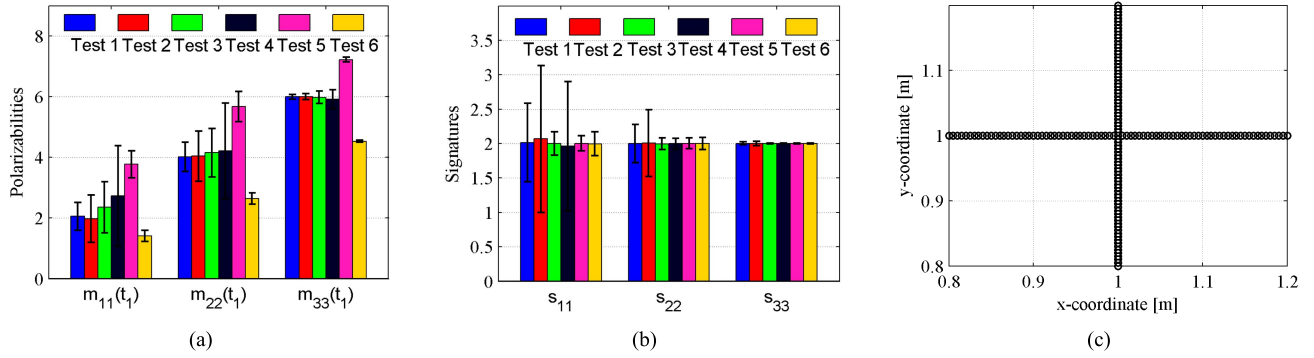

Fig. 4.   (a) Effects of different sources of uncertainties on the estimation of target principal polarizabilities $m_{11}(t_1)$, $m_{22}(t_1)$, and $m_{33}(t_1)$ (mean values and standard deviations $\pm 2\sigma$) in a circular multicoil sensor. (b) Effects of different sources of uncertainties on the estimation of target principal signatures s_{11}, s_{22}, and s_{33} (mean values and standard deviations $\pm 2\sigma$) in a circular multicoil sensor. (c) Trajectory of the target during scan in a circular multicoil sensor.
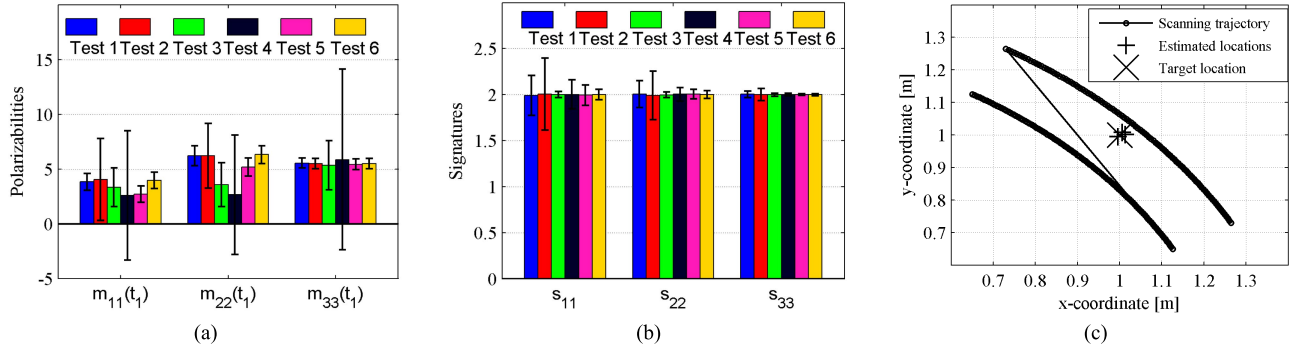

Fig. 5.   (a) Effects of different sources of uncertainties on the estimation of target principal polarizabilities $m_{11}(t_1)$, $m_{22}(t_1)$, and $m_{33}(t_1)$ (mean values and standard deviations $\pm 2\sigma$) in an octagonal monocoil sensor. (b) Effects of different sources of uncertainties on the estimation of target principal signatures s_{11}, s_{22}, and s_{33} (mean values and standard deviations $\pm 2\sigma$) in an octagonal monocoil sensor. (c) Trajectory of the sensor coil during scan, actual target position, and estimates of target position obtained from tests 1–6 in an octagonal monocoil sensor.

TABLE II
SPECIFICATIONS FOR TESTING THE ALGORITHM FOR THE ESTIMATION OF
TARGET PRINCIPAL POLARIZABILITIES AND PRINCIPAL SIGNATURES
WITH RESPECT TO SENSOR UNCERTAINTIES

Test no.	Meas. noise, SNR_m (dB)	Pos. noise, SNR_p (dB)	Coil geometry vector, G_v (m) Circular multi-coil sensor	Coil geometry vector, G_v (m) Octagonal mono-coil sensor
1	30	40	[0.15 0.06 0.04]	[0.12 0.06 0.09 0.06]
2	25	40	[0.15 0.06 0.04]	[0.12 0.06 0.09 0.06]
3	40	30	[0.15 0.06 0.04]	[0.12 0.06 0.09 0.06]
4	40	25	[0.15 0.06 0.04]	[0.12 0.06 0.09 0.06]
5	40	40	[**0.17** 0.06 0.04]	[**0.14** 0.06 0.09 0.06]
6	40	40	[0.15 0.06 **0.05**]	[0.12 0.06 **0.11** 0.06]

was used as a target. The sensor was fixed at (1 m, 1 m, 0 m) and the target was moved in a cross-like pattern within the xy plane 5 cm above the sensor [Fig. 4(c)]. The scanning scheme with a fixed sensor and a moving target was chosen in order to match the actual laboratory experiment procedure. The obtained results are shown in Fig. 4(a) and (b).

For the octagonal coil sensor, two arc-shaped sensor scans with $0.3°$ angular resolution and a constant sensor height of 0.1 m were used to interrogate the dipole target (featuring the same polarizability vectors), fixed at (1 m, 1 m, −0.01 m) [Fig. 5(c)]. Such a sweeping pattern simulates a field experiment scenario in which the sensor is swept

by the 2-DoF robotic arm. The obtained results are shown in Fig. 5(a) and (b).

In both cases, the scanning patterns were chosen with respect to the spatial distribution of the sensor x-, y-, and z-directions sensitivities. From Figs. 2 and 3, it is evident that the maximal scan range needed for the estimation of m_{ii} and s_{ii} is primarily determined by the size of sensor coils. The coil size is also a parameter that dominantly affects the maximal depth at which a target can be detected and characterized. In HD applications, targets typically need to be detected up to a depth of 20 cm [3], so the geometries of sensor coils and the scan range need to be set accordingly. Besides the sensitivity distribution, another criterion for the selection of scanning patterns was the ability to investigate the effects of limited spatial diversity of data. This is an important feature since normally much larger and denser sweeping grids are used for the full dipole model reconstruction [42].

C. Discussion

Tests 1 and 2 show the effects of measurement noise while the positioning noise SNR is held constant. For both sensors [Figs. 4 (a) and (b) and 5(a) and (b)], it can be observed that the mean values and standard deviations of m_{ii} and s_{ii} are almost equally affected. This seems to be in contradiction with our previous assumptions on the mutual cancellation of different sensor uncertainties when using s_{ii} instead of m_{ii}. However, this can be explained by the fact that at SNR levels approaching 25 dB and below, the estimation algorithm
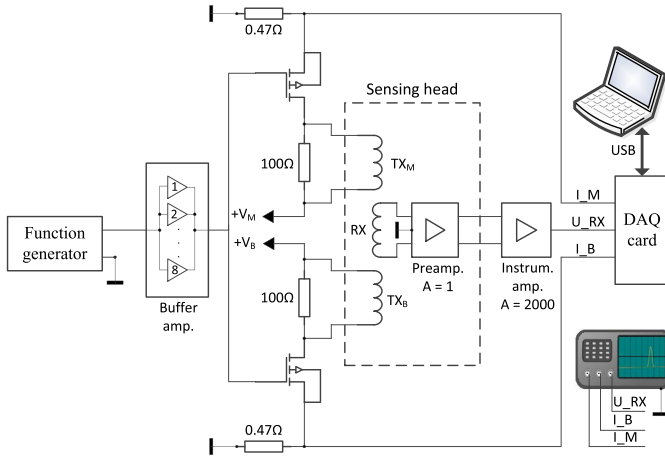
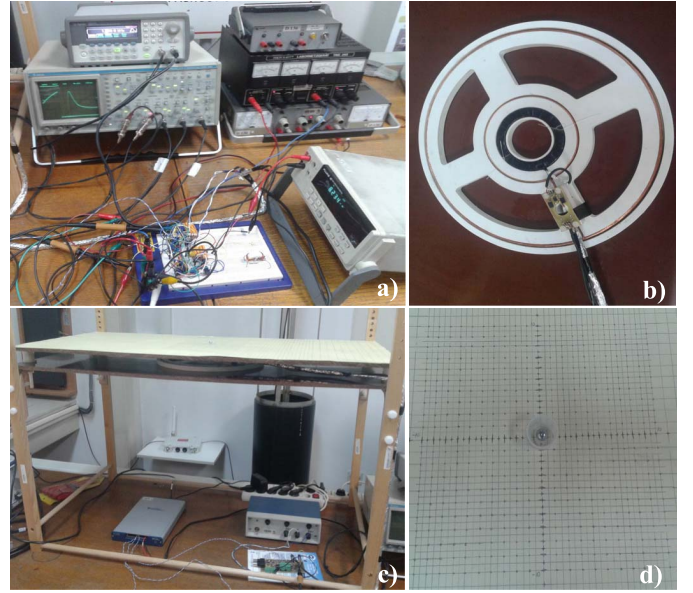Fig. 6.   Functional block diagram of the experimental sensor platform.

Fig. 7.   Experimental setup. (a) Electronic instrumentation and prototyping hardware. (b) Sensing head with preamplifier board. (c) Testing stand. (d) xy scanning grid.

effectiveness decreases significantly, since lower sensitivities in the x- and y-directions (compared with the z-direction) start to affect the invertibility of the sensitivity matrix $\mathbf{H}_{xyz}$. However, since the SNR is defined over a signal used for inversion (not at the signal chain input), lower SNR levels might be tolerated in practice.

Tests 3 and 4 and 5 and 6 show the effects of positioning noise and the uncertainties in coil geometry, respectively, while the measurement noise SNR is held constant. For both sensors, these uncertainties propagate heavily to m_{ii}, whereas s_{ii} remain stable, as expected. For a given scan range, the SNR level of 25 dB corresponds to the positioning uncertainty higher than 1 cm (test 4), which is larger than the actual requirements for the accuracy of positioning systems needed for HD [22], [23]. This proves the robustness and practical applicability of the algorithm. Different propagations of uncertainties to m_{ii} and s_{ii} of each sensor reflect different test schemes (moving sensor versus moving target) as well as different sensor sensitivities.

V. Validation on an Experimental Sensor Platform

The first stage of an experimental validation of the proposed algorithm was conducted in a controlled laboratory environment. For that purpose, an experimental sensor platform was developed and used with different metal test samples of known geometric and material properties.

A. Experimental Setup

A basic diagram depicting the main functional blocks of the experimental sensor platform is shown in Fig. 6. The physical implementation of the whole setup is shown in Fig. 7.

The sensing part of the platform is the search head [Fig. 7(b)] consisting of three circular coils [Fig. 1(a)]. TX_M coil has a radius of 15 cm and 12 turns, TX_B coil has a radius of 6 cm and 4 turns, and the RX coil has a radius of 4 cm and 200 turns. The RX coil is shielded in order to reduce the capacitive coupling from the TX side. The resonant frequency is over 1 MHz for TX coils and around 350 kHz for the RX coil.

The pulse excitation signal (pulse duration 50 μs, frequency 1 kHz, and magnitude 10 V) is provided from a function generator (Agilent 33250A) and simultaneously fed to two coil-driving MOSFETs (IRF830) via digital buffer amplifiers (CD4050). MOSFETs with high breakdown voltage (500 V) are used for high-speed switching of coil current. Resistors in parallel to each of the coils prevent the oscillations in the TX circuit. Each MOSFET is powered from a separate dc power source ($+V_M$, $+V_B$), so that driving current magnitudes of TX_M and TX_B coils can be controlled independently. In effect, TX_M and TX_B coils are driven with synchronized current pulses of opposite polarity (magnitudes 2.3 and 2 A, respectively). This is important in order to achieve better sensor balancing. A well-balanced TD sensor means that the transient voltage spike induced in the RX coil immediately after the TX current has been switched off decays as quickly as possible (typically within 2–10 μs [43]) so that the response of a metal target can be captured within a dynamic range of a receiver amplifier. Measuring the target response at early times (typically 10–30 μs after the excitation switch off) is needed for small metal targets, such as low-metal content landmines.

The RX part of a sensor platform consists of a preamplifier with differential output located near the coils ($A = 1$, Texas Instruments, OPA1612) and an instrumentation amplifier ($A = 2000$, Texas Instruments, INA166). The signal from the RX amplifier together with signals corresponding to excitation currents in TX_M and TX_B coils is fed to the analog inputs of a 16-bit data acquisition card (National Instruments, USB-6366), sampled at 2 MS/s/channel and processed on a PC using MATLAB. For each measurement channel, data from 64 excitation pulse periods are averaged in order to obtain a better SNR, resulting in a 64-ms averaging period.

B. Test Targets

Several different metal test samples were used for testing the shape estimation algorithm. Specifications of their type and geometric and material properties are given in Table III.

TABLE III

SPECIFICATION OF TEST TARGETS USED WITH THE
EXPERIMENTAL SENSOR PLATFORM

Target no.	Geometric properties	Material properties
1	Sphere, diameter 15 mm	Magn. steel, DIN 13505
2	Sphere, diameter 12 mm	Magn. steel, DIN 13505
3	Cylinder, Ø8 mm x 24 mm	Magn. steel, DIN 13505
4	Hexagonal nut, M12	Galvanized magn. steel
5	Nut washer, M14	Galvanized magn. steel

C. Testing Procedure

All tests were conducted on a nonmetallic testing stand, 0.5 m above the working surface, so that the effects of nearby conducting/magnetic objects were excluded [Fig. 7(c)]. The sensing head was held fixed at the bottom plate and targets were manually positioned on an xy grid (size 10 cm × 10 cm, resolution 0.5 cm) located on the upper plate 5 cm above the coils. Such a configuration was used for practical reasons, so that the wiring and instrumentation of the search head remains at a fixed position. At each target position, the measurements in air (zero signal) were taken and then subtracted from the target response in order to compensate for sensor drift effects.

D. Experiments and Results

Typical waveforms that correspond to different test targets, located at (0 cm, 0 cm, 5 cm), are shown in Fig. 8. The measurement window starts at 15 μs after the excitation switch off, as the RX amplifier exits the saturation stage. Data are taken at three TGs: 1) $t_1 = 16$ μs; 2) $t_2 = 19$ μs; and 3) $t_3 = 22$ μs. The TGs are carefully chosen in order to capture the portion of the pulse decay curve suitable for calculation of the signature matrix.

Sensor responses corresponding to test targets 1–5 (Table III) are shown in Figs. 9 and 10, respectively. Measurements acquired at TGs t_1–t_3 are concatenated on the same graph for each target. For each measured signal, estimated sensor response (i.e., response reconstructed from inverted magnetic polarizability tensor and target location at a given TG) is also shown in order to validate the fit between the measured data and model prediction. For each target, the same xy scanning pattern was used [Fig. 10(c)]. Five measurement cycles were conducted for each target type in order to validate the measurement repeatability. Based on the obtained sensor responses, corresponding signature matrices **S** were calculated, and the mean value and standard deviation of each matrix element were obtained (Table IV).

E. Discussion

Based on sensor responses to test targets 1–5, the results from Table IV clearly indicate that the signature matrix elements are in general consistent with the expected magnetic ratios of individual targets. The obtained signature matrices of the two spherical targets are very close to a unity matrix. For the other targets, the matrix elements clearly indicate the dominant PAs (z-direction for the cylindrical target, the equally dominant x- and y-directions for the hexagonal nut and the
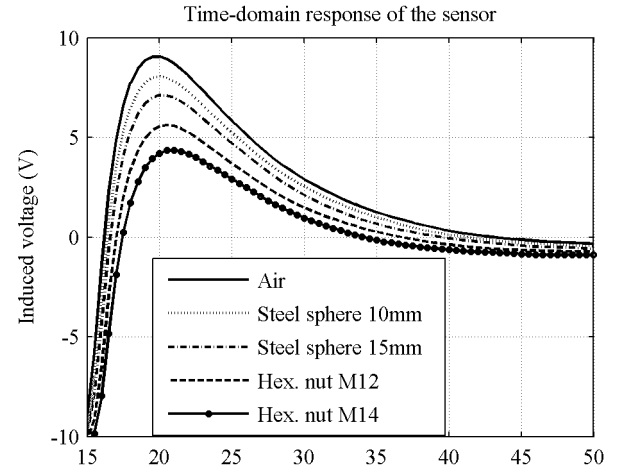

Fig. 8. Typical sensor waveform in response to different targets. Three characteristic TGs are selected for the calculation of the signature matrix.

nut washer, respectively). All targets were oriented vertically, except for the nut washer, whose symmetry axis was in the y-direction. The uncertainty levels ($\pm 2\sigma$) of the obtained aspect ratios are under $\pm 5\%$ for all targets, which are comparable with the simulation results. Manual positioning of targets on an xy grid and the simplified coil model [Fig. 1(a)] were the main sources of uncertainties introduced in the experiments.

VI. VALIDATION ON A MOBILE
METAL DETECTOR PLATFORM

After the first stage of experimental validation in laboratory environment, the proposed estimation algorithm was also tested in field conditions in order to validate its effectiveness for a targeted application. The experiments were conducted on a specific mobile platform consisting of a commercial MD and a mobile robot (Fig. 11). The platform was used in a robot competition event aiming to promote the development of new strategies for autonomous landmine detection using mobile ground robots [44], [45], with a support and partnership from the EU FP7 TIRAMISU project [46].

A. Metal Detector

A central part of the mobile detection system is the Vallon VMP3, a TD three-coil MD [Fig. 1(b)] [48]. For each of the three coils of VMP3, data corresponding to induced voltages sampled at three different TGs are made available to the robot. For each detection signal, a reference (zero) signal corresponding to the same coil and TG was provided. The reference signal basically corresponds to sensor readings acquired at the default sensor height over the ground (i.e., liftoff) with no targets present. Such information is used for simple soil compensation. Raw sensor data are filtered within the VMP3 and updated at the rate of 10 Hz/channel.

B. Mobile Robot

The Clearpath Husky A200 robot was used as an autonomous scanning platform [49]. The robot comprises sensing systems for localization, navigation, and obstacle avoidance, such as stereo cameras, laser range finder, real-time kinematic global positioning system, inertial measurement unit, and odometry sensors. A 2-DoF robotic arm is used
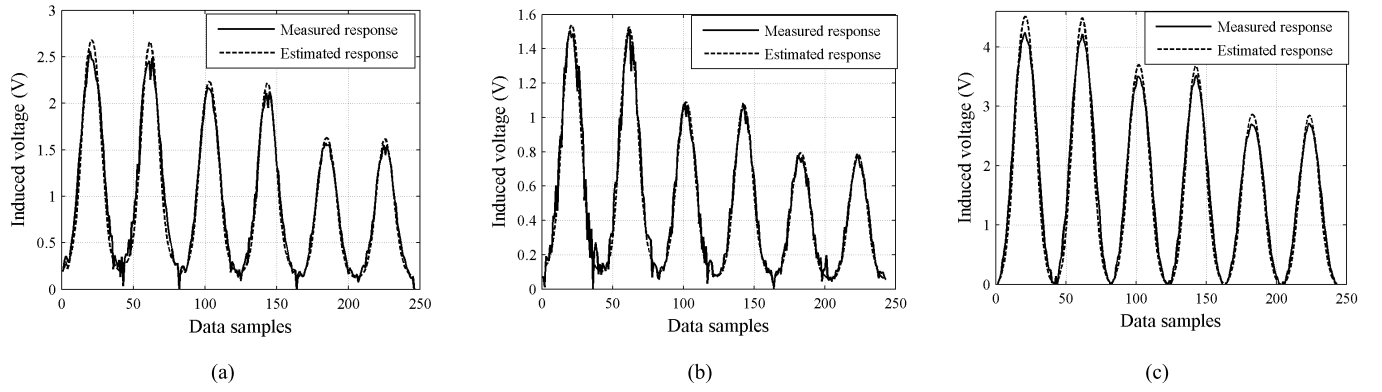
Fig. 9. Measured and estimated sensor responses. a) Test target 1 (sphere of diameter 15 mm). b) Test target 2 (sphere of diameter 12 mm). c) Test target 3 (cylinder of Ø8 mm × 24 mm).
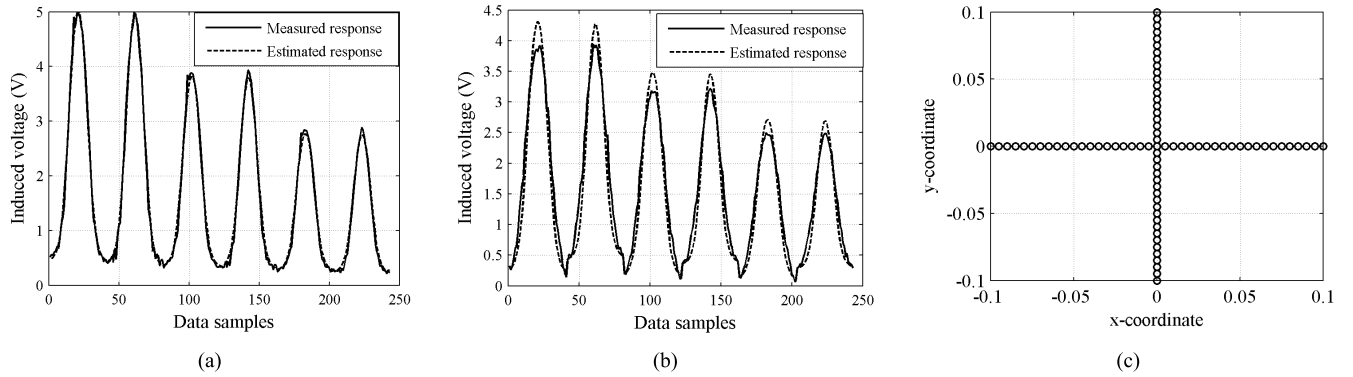

Fig. 10. Measured and estimated sensor responses. a) Test target 4 (hexagonal nut M12). b) Test target 5 (nut washer M14). c) Trajectory of the target during the scan.

TABLE IV

ESTIMATED ELEMENTS OF SIGNATURE MATRICES OF TEST TARGETS 1–5 (MEAN VALUES AND STANDARD DEVIATIONS $\pm 2\sigma$)

Signature matrix element	Test target 1 (sphere, diameter 15 mm)		Test target 2 (sphere, diameter 12 mm)		Test target 3 (cylinder Ø8 mm x 24 mm)		Test target 4 (hexagonal nut M12)		Test target 5 (nut washer M14)	
	Mean val.	*Std. dev.*	*Mean val.*	*Std. dev.*	*Mean val.*	*Std. dev.*	*Mean val.*	*Std. dev.*	*Mean val.*	*Std. dev.*
s_{11}	0.948	0.039	0.933	0.051	1.043	0.046	1.120	0.036	1.346	0.056
s_{21}	0.914	0.043	0.900	0.047	0.985	0.037	1.016	0.047	1.294	0.062
s_{31}	0.964	0.032	0.965	0.049	0.964	0.041	0.939	0.056	1.250	0.059
s_{12}	0.999	0.046	0.954	0.038	1.424	0.063	0.895	0.043	1.243	0.048
s_{22}	0.979	0.037	0.934	0.029	1.310	0.058	0.872	0.037	1.210	0.039
s_{23}	0.980	0.021	0.979	0.041	1.221	0.063	0.853	0.029	1.183	0.061
s_{13}	1.052	0.029	1.022	0.042	1.364	0.054	0.800	0.034	0.923	0.047
s_{23}	1.070	0.053	1.037	0.049	1.330	0.049	0.859	0.021	0.935	0.052
s_{33}	1.017	0.048	1.014	0.050	1.304	0.057	0.908	0.039	0.946	0.038

for sweeping the MD over the target area. The pose of each coil is updated at the rate of 50 Hz and is synchronized with the MD readings. Since the sensor pose is obtained through the fusion of data from arm positioning and robot navigation sensors, its update rate depends on update rates of individual sensors and the implementation of the fusion algorithm. The sensor data rate is determined by the VMP3 only.

A basic block diagram depicting main parts of the mobile MD platform and signals used for the implementation of the target shape estimation algorithm is shown in Fig. 12.

C. Test Targets

In order to validate the proposed shape estimation method, the algorithm was tested with data sets obtained from field trials of the mobile scanning platform. Two types of targets were used as surrogate mines: steel spheres (diameter 1 cm) [Fig. 13(a)] and hexagonal nuts made of galvanized

This article has been accepted for inclusion in a future issue of this journal. Content is final as presented, with the exception of pagination.

10   IEEE TRANSACTIONS ON INSTRUMENTATION AND MEASUREMENT

Fig. 11. Clearpath Husky mobile robot with the Vallon VMP3 MD [47]. (Photo from the HRATC 2014 event.)
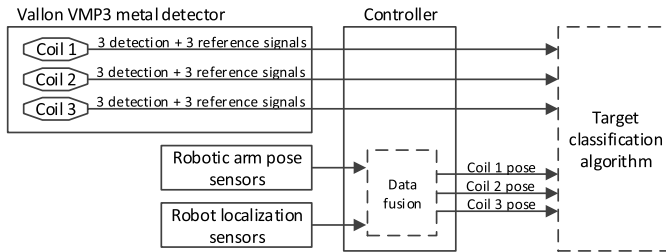
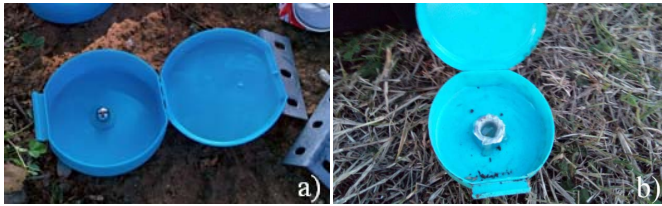Fig. 12. Block diagram of the mobile MD platform.

Fig. 13. Testing targets. (a) Steel sphere. (b) Magnetic hexagonal nut [50], [51]. (Photos from HRATC 2014/2015 events.)

(magnetic) steel [Fig. 13(b)]. All targets were placed inside a plastic package and buried at random locations near the soil surface.

D. Testing Procedure

All experiments involving the mobile detection platform and test targets were conducted during field trials, held at a remote location, within a framework of the robot competition event [44], [45]. The primary purpose of these trials was to test that the robot navigation and landmine detection algorithms, developed by teams participating in the event, are in line with the event's objectives and rules. Due to the nature of such experiments held without actual presence of the participants, the authors of this paper had no means of controlling or moderating the experiments. For that reason, we used only the data sets containing sensor responses to targets from Fig. 13, sensor and robot poses, as well as ground-truth tables (where available) and tested our algorithms offline.

Before actually using the data sets for algorithm validation, a special model calibration procedure was performed. Since the VMP3 sensor was not physically available, and only its coarse dimensions and the outer shape of its search head were known, parameters of the octagonal coil geometry model [Fig. 1(b)] had to be somehow estimated before the

same model is used again for target shape estimation. For that purpose, we used a portion of the testing data set that was known to contain sensor response to a steel sphere. We developed a nonlinear optimization algorithm, similar to the one described in Table I, and estimated the sensor geometry vector $\mathbf{G}_D$ and constant k by fitting the measured data with the model response in a least-squares sense. These geometry parameters were then used for all subsequent experiments involving shape estimations of different targets with different spatial sweeps.

The field experiments were conducted over a soil with moderate effects on MD performance, meaning that its effects were notable but the MD could be used without ground compensation [39]. In the testing data sets, small dc offsets caused by varying sensor liftoff were observed and corrected.

E. Experiments and Results

Sensor readings corresponding to voltages induced in the left sensor coil (acquired at three different TGs) in response to a buried steel sphere are given in Fig. 14, respectively. For each signal, the estimated sensor response (i.e., response reconstructed from inverted magnetic polarizability tensor and target location at a given TG) is also shown in order to validate the the fit between the measured data and model prediction. Responses from the other two coils were not shown due to low detection signals. Fig. 16(a) shows the xy trajectory of the left sensor coil during the scan, with the estimated initial and final target locations.

Figs. 15(a)–(c) present the sensor readings and a reconstructed signal of a sensor coil in response to a buried hexagonal nut, also for three different TGs. The corresponding sensor coil trajectory and the estimated initial and final target positions are shown in Fig. 16(b). Based on data sets containing sensor responses to targets from Fig. 13, corresponding signature matrices $\mathbf{S}$ were calculated. For each target type, five different data subsets were used [with sensor responses and scanning patterns similar to those in Figs. 14–16(a) and (b)], and the mean value and standard deviation of each matrix element were obtained. The results are shown in Fig. 16(c) as magnetic aspect ratios.

F. Discussion

Based on data sets containing sensor responses to steel spheres, the results clearly indicate that matrix elements that rely on TG t_1 and t_2 only (i.e., the first row elements of $\mathbf{S}$) show a very good agreement with theoretical values [Fig. 16(c)]. On the other hand, other matrix elements that take into account tensor eigenvalues inverted at t_3 show significant discrepancy and are clearly not feasible for practical shape estimation purposes.

One possible explanation of such results would be that the sensor readings at t_3 may already reside outside intermediate time portion of the decay curve (and presumably somewhere within the late time portion), where (15) is no longer valid for the estimation of magnetic aspect ratios. This remains an open question, since for VMP3, no information on the exact timing properties of sensor response (such as those shown in Fig. 8)
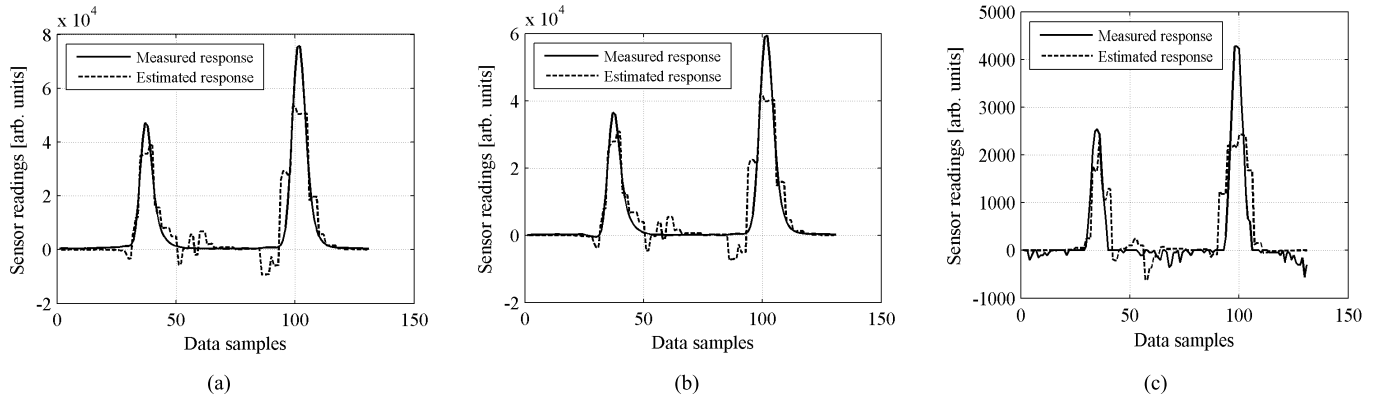
This article has been accepted for inclusion in a future issue of this journal. Content is final as presented, with the exception of pagination.

AMBRUŠ *et al.*: ROBUST ESTIMATION OF METAL TARGET SHAPE USING TD EMI DATA   11

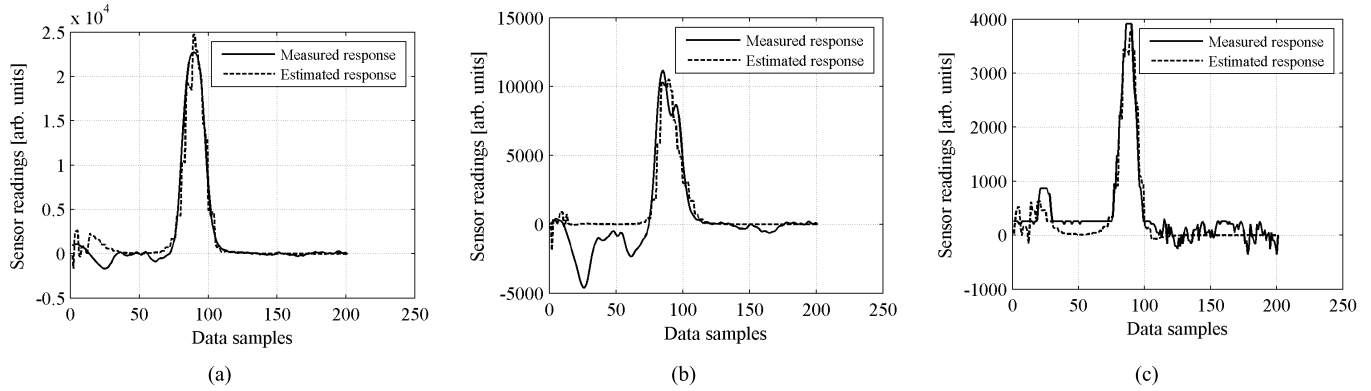Fig. 14.   Measured and estimated sensor responses to a buried sphere recorded at a left coil at 3 TGs. a) TG t_1. b) TG t_2. c) TG t_3.

Fig. 15.   Measured and estimated sensor responses to a buried hexagonal nut recorded at a left coil at 3 TGs. a) TG t_1. b) TG t_2. c) TG t_3.
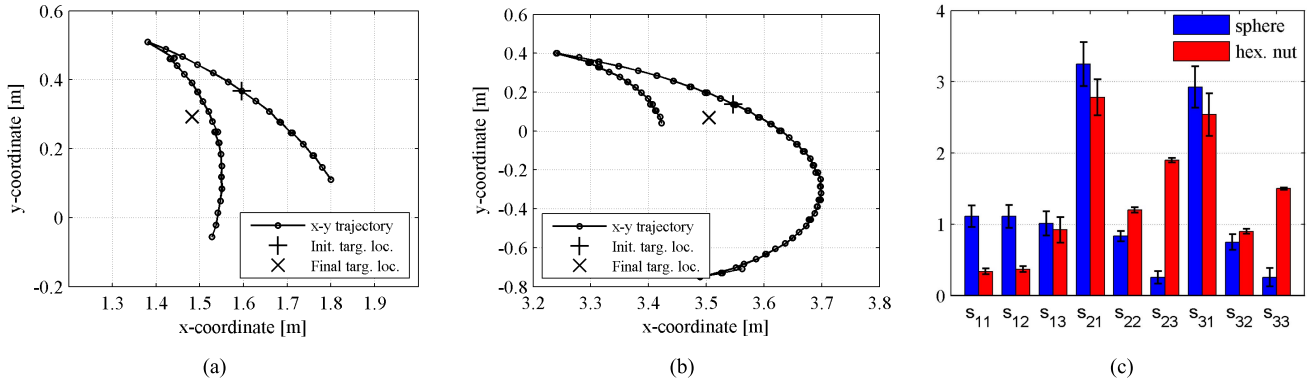

Fig. 16.   Trajectory of the left sensor coil during scan and the estimated target position (initial guess and final inverted position). a) Sphere. b) Nut. c) Estimated elements of signature matrices of the sphere and the nut (mean values and standard deviations $\pm 2\sigma$).

was available. In general, sensor readings from more than two TGs could provide more reliable shape information, if these readings are taken at carefully chosen time instances (e.g., in the intermediate part of the pulse decay response).

The obtained signature matrix of a hexagonal nut suggests that its first row elements are in general consistent with expected magnetic aspect ratios. Since the nut has two equally dominant PA in the x- and y-directions and a less dominant PA in the z-direction, the s_{11}/s_{22} is approximately equal to 1, while the other two signature ratios are lower than 1, as expected.

Fig. 16(c) also shows that the uncertainty levels ($\pm 2\sigma$) of the obtained aspect ratios are under $\pm 15\%$ for both targets, which are comparable with the results obtained by simulations. This suggests that these parameters could potentially serve

as simple and reliable shape-based classifiers in scenarios where data of limited spatial diversity and sensor uncertainties would prohibit the use of more sophisticated algorithms, such as those based on full polarizability tensor reconstruction or inductive imaging. The main limitation of the method is that it works on magnetic metal targets only, which narrows its potential application in HD, but opens up other areas such as small ordnance detection.

G. Future Work

In our future work, we plan to test the algorithm in field conditions with more sensor data corresponding to similar sized magnetic metal targets of different shapes, similar to those used in the laboratory experiments. We also plan to

implement the algorithm for real-time operation on a mobile platform, which is feasible due to the use of relatively simple and computationally efficient analytic forward models and inversion algorithms. In our offline implementation on a desktop PC, the execution time of the classifier algorithm was around 2 s for an average sensor data set of 100–200 samples. A similar algorithm performance could be expected for a targeted implementation on an embedded controller of a mobile robot featuring ROS operating system [52].

VII. Conclusion

A novel model-based algorithm for general shape estimation of buried metal targets using TD EMI data was presented. The algorithm features an application of a signature matrix, a simple and robust parameter that relies on temporal information contained in the target's principal magnetic polarizabilities rather than their magnitudes, making it a very robust solution for target shape estimation and classification. The proposed algorithm was evaluated using two different sensor platforms, both through simulations and experiments.

Tests conducted in laboratory conditions using an experimental sensor platform and different test targets of known geometric and material properties confirmed the soundness and basic applicability of the proposed approach. The results clearly indicate that the target shape can be estimated from the sensor data with a limited spatial coverage and under the uncertainties related to the sensor positioning and coil geometry. This leads to an application of the signature matrix for simple and reliable shape-based target classification in scenarios where the use of more sophisticated algorithms, such as those based on full polarizability tensor reconstruction or inductive imaging, would not be feasible.

Method validation was also performed in field conditions using a mobile MD platform. Although the field tests provided limited data quantity of only two (useful) target types, the targets were successfully discriminated with the estimation of a portion of the signature matrix. The results confirm that the method has a strong potential to be implemented in robotic systems for buried target detection and classification.

The main limitation of the proposed approach is that it can be applied only to magnetic metal targets, which narrows its potential application in HD, but opens up other application areas such as small ordnance detection or nondestructive testing. The effects of material properties (electrical conductivity and magnetic permeability) on the estimation of target shape using the proposed approach is another area of research that still needs to be further investigated.

Acknowledgment

References

[1] *UNMAS Annual Report 2013, United Nations Mine Action Service.* [Online]. Available: http://www.mineaction.org, accessed Aug. 6, 2015.

[2] K. Furuta and J. Ishikawa, Eds., *Anti-Personnel Landmine Detection for Humanitarian Demining*. London, U.K.: Springer-Verlag, 2009.

[3] D. Guelle, A. Smith, A. Lewis, and T. Bloodworth, *Metal Detector Handbook for Humanitarian Demining*. Norwich, U.K.: Office for Official Publications of the European Communities, 2003.

[4] L. Marques *et al.*, "Sensors for close-in detection of explosive devices current status and future prospects," in *Proc. 9th Int. Symp. Humanitarian Demining*, 2012, pp. 147–151.

[5] S. Baglio, L. Cantelli, F. Giusa, and G. Muscato, "Intelligent prodder: Implementation of measurement methodologies for material recognition and classification with humanitarian demining applications," *IEEE Trans. Instrum. Meas.*, vol. 64, no. 8, pp. 2217–2226, Aug. 2015.

[6] T. M. Grzegorczyk, J. P. Fernández, F. Shubitidze, K. O'Neill, and B. E. Barrowes, "Subsurface electromagnetic induction imaging for unexploded ordnance detection," *J. Appl. Geophys.*, vol. 79, pp. 38–45, Apr. 2012.

[7] S. Nazlibilek, O. Kalender, and Y. Ege, "Mine identification and classification by mobile sensor network using magnetic anomaly," *IEEE Trans. Instrum. Meas.*, vol. 60, no. 3, pp. 1028–1036, Mar. 2011.

[8] J. P. Fernandez, B. E. Barrowes, T. M. Grzegorczyk, N. Lhomme, K. O'Neill, and F. Shubitidze, "A man-portable vector sensor for identification of unexploded ordnance," *IEEE Sensors J.*, vol. 11, no. 10, pp. 2542–2555, Oct. 2011.

[9] S. L. Tantum, W. R. Scott, K. D. Morton, L. M. Collins, and P. A. Torrione, "Target classification and identification using sparse model representations of frequency-domain electromagnetic induction sensor data," *IEEE Trans. Geosci. Remote Sens.*, vol. 51, no. 5, pp. 2689–2706, May 2013.

[10] M. D. Tran, C. Abeynayake, and L. C. Jain, "A target discrimination methodology utilizing wavelet-based and morphological feature extraction with metal detector array data," *IEEE Trans. Geosci. Remote Sens.*, vol. 50, no. 1, pp. 119–129, Jan. 2012.

[11] C. E. Baum, "Low frequency near-field magnetic scattering from highly conducting, but not perfectly conducting bodies," in *Detection and Identification of Visually Obscured Targets*, C. E. Baum, Ed. Philadelphia, PA, USA: Taylor & Francis, 1999, ch. 6, pp. 163–217.

[12] T. H. Bell, B. J. Barrow, and J. T. Miller, "Subsurface discrimination using electromagnetic induction sensors," *IEEE Trans. Geosci. Remote Sens.*, vol. 39, no. 6, pp. 1286–1293, Jun. 2001.

[13] L. R. Pasion and D. W. Oldenburg, "Locating and determining dimensionality of UXO using time domain electromagnetic induction," in *Proc. Symp. Appl. Geophys. Eng. Environ. Prob.*, vol. 12. 1999, pp. 763–772.

[14] J. T. Smith and H. F. Morrison, "Estimating equivalent dipole polarizabilities for the inductive response of isolated conductive bodies," *IEEE Trans. Geosci. Remote Sens.*, vol. 42, no. 6, pp. 1208–1214, Jun. 2004.

[15] S. J. Norton and I. J. Won, "Identification of buried unexploded ordnance from broadband electromagnetic induction data," *IEEE Trans. Geosci. Remote Sens.*, vol. 39, no. 10, pp. 2253–2261, Oct. 2001.

[16] T. M. Grzegorczyk and B. E. Barrowes, "Real-time processing of electromagnetic induction dynamic data using Kalman filters for unexploded ordnance detection," *IEEE Trans. Geosci. Remote Sens.*, vol. 51, no. 6, pp. 3439–3451, Jun. 2013.

[17] B. Dekdouk, L. A. Marsh, D. W. Armitage, and A. J. Peyton, "Estimating magnetic polarizability tensor of buried metallic targets for land mine clearance," in *Ultra-Wideband, Short-Pulse Electromagnetics 10*. New York, NY, USA: Springer-Verlag, 2014, pp. 425–432.

[18] L. A. Marsh, C. Ktistis, A. Järvi, D. W. Armitage, and A. J. Peyton, "Three-dimensional object location and inversion of the magnetic polarizability tensor at a single frequency using a walk-through metal detector," *Meas. Sci. Technol.*, vol. 24, no. 4, pp. 045102-1–045102-13, 2013.

[19] Y. Zhao, W. Yin, C. Ktistis, D. Butterworth, and A. J. Peyton, "On the low-frequency electromagnetic responses of in-line metal detectors to metal contaminants," *IEEE Trans. Instrum. Meas.*, vol. 63, no. 12, pp. 3181–3189, Dec. 2014.

[20] J. T. Smith and H. F. Morrison, "Optimizing receiver configurations for resolution of equivalent dipole polarizabilities *in situ*," *IEEE Trans. Geosci. Remote Sens.*, vol. 43, no. 7, pp. 1490–1498, Jul. 2005.

[21] C. P. Oden, "Combining advances in EM induction instrumentation and inversion schemes for UXO characterization," *Prog. Electromagn. Res. B*, vol. 38, pp. 107–134, Jan. 2012.

This article has been accepted for inclusion in a future issue of this journal. Content is final as presented, with the exception of pagination.

AMBRUŠ *et al.*: ROBUST ESTIMATION OF METAL TARGET SHAPE USING TD EMI DATA

13

[22] A. B. Tarokh and E. L. Miller, "Subsurface sensing under sensor positional uncertainty," *IEEE Trans. Geosci. Remote Sens.*, vol. 45, no. 3, pp. 675–688, Mar. 2007.

[23] L. Beran, S. Billings, and D. Oldenburg, "Robust inversion of time-domain electromagnetic data: Application to unexploded ordnance discrimination," *J. Environ. Eng. Geophys.*, vol. 16, no. 3, pp. 127–141, Sep. 2011.

[24] H. Bergeler, H. Ewald, H. Krambeer, and E. Kubota, "Optical position monitoring using spatial filters for improved magnet-inductive prospection of metal pieces," *Proc. SPIE 5826, Opto-Ireland Opt. Sensing Spectrosc.*, p. 679, Jul. 2005. [Online]. Available: http://dx.doi.org/10.1117/12.606159

[25] H. Krüger, "Solutions for 3D position referencing for handheld metal detectors used in humanitarian demining," in *Proc. IEEE Instrum. Meas. Technol. Conf. (I2MTC)*, May 2010, pp. 447–451.

[26] A. Sheinker, B. Ginzburg, N. Salomonski, L. Frumkis, and B.-Z. Kaplan, "Localization in 3-D using beacons of low frequency magnetic field," *IEEE Trans. Instrum. Meas.*, vol. 62, no. 12, pp. 3194–3201, Dec. 2013.

[27] P. Nováček, J. Roháč, and P. Ripka, "Complex markers for a mine detector," *IEEE Trans. Magn.*, vol. 48, no. 4, pp. 1489–1492, Apr. 2012.

[28] D. Portugal, L. Marques, and M. Armada, "Deploying field robots for humanitarian demining: Challenges, requirements and research trends," in *Proc. 17th Int. Conf. Climbing Walking Robots (CLAWAR)*, 2014, pp. 649–656.

[29] L. Li *et al.*, "Cart-mounted geolocation system for unexploded ordnance with adaptive ZUPT assistance," *IEEE Trans. Instrum. Meas.*, vol. 61, no. 4, pp. 974–979, Apr. 2012.

[30] D. A. Grejner-Brzezinska, C. K. Toth, H. Sun, X. Wang, and C. Rizos, "A robust solution to high-accuracy geolocation: Quadruple integration of GPS, IMU, pseudolite, and terrestrial laser scanning," *IEEE Trans. Instrum. Meas.*, vol. 60, no. 11, pp. 3694–3708, Nov. 2011.

[31] J. Jumadinova and P. Dasgupta, "Multirobot autonomous landmine detection using distributed multisensor information aggregation," *Proc. SPIE 8407, Multisensor, Multisource Inf. Fusion, Architect., Algorithms, Appl.*, p. 84070B, May 2012.

[32] A. M. Kaneko, G. Endo, and E. F. Fukushima, "Landmine buried depth estimation by curve characterization of metal mine detector signals," in *Proc. IEEE Conf. Intell. Robots Syst. (IROS)*, Nov. 2013, pp. 5327–5332.

[33] A. M. Kaneko and E. F. Fukushima, "Development of an automatic land-mine detection and marking system for the demining robot gryphon," *J. Adv. Comput. Intell. Intell. Informat.*, vol. 15, no. 6, pp. 737–743, 2011.

[34] M. Freese, E. F. Fukushima, and S. Hirose, "Improved landmine discrimination with an off-the-shelf metal detector," *J. Mine Action*, vol. 12, no. 1, pp. 1–8, 2008. [Online]. Available: http://www.jmu.edu/cisr/journal/12.1/rd/freese/freese.shtml

[35] T. Bell, "Phenomenology and signal processing for UXO/clutter discrimination," Strategic Environ. Res. Develop. Program, Project Rep. MM-1595, Aug. 2009. [Online]. Available: https://www.serdp-estcp.org/Program-Areas/Munitions-Response/Land/Modeling-and-Signal-Processing/MR-1595.

[36] D. Ambruš, D. Vasić, and V. Bilas, "Active induction balance method for metal detector sensing head utilizing transmitter-bucking and dual current source," *J. Phys., Conf. Ser.*, vol. 450, no. 1, p. 012047, 2013.

[37] R. Georgieva. *Metal Detectors Coil and Search Head Design—Patents and Utility Models*, DeepTech Metal Detectors. [Online]. Available: http://www.deeptech-bg.com/search_coils.pdf, accessed Aug. 6, 2015.

[38] H. Keller, "Arrangement and method for detecting metal objects," European Patent 0 654 685 A3, Dec. 20, 1995.

[39] *Humanitarian Mine Action—Test and Evaluation—Part 2: Soil Characterization for Metal Detector and Ground Penetrating Radar Performance*, CEN Standard CWA 14742-2, Aug. 2008.

[40] T. H. Bell, B. Barrow, and N. Khadr, "Shape-based classification and discrimination of subsurface objects using electromagnetic induction," in *Proc. IEEE Int. Geosci. Remote Sens. Symp. (IGARSS)*, vol. 1. Jul. 1998, pp. 509–513.

[41] D. Ambruš, D. Vasić, and V. Bilas, "Model-based target classification using spatial and temporal features of metal detector response," in *Proc. IEEE Sensors Appl. Conf. (SAS)*, Apr. 2015, pp. 1–6.

[42] L. R. Pasion, "Inversion of time domain electromagnetic data for the detection of unexploded ordnance," Ph.D. dissertation, Dept. Geophys., Univ. Brit. Columbia, Vancouver, BC, Canada, Aug. 2007.

[43] C. V. Nelson, C. V. Cooperman, W. Schneider, D. S. Wenstrand, and D. G. Smith, "Wide bandwidth time-domain electromagnetic sensor for metal target classification," *IEEE Trans. Geosci. Remote Sens.*, vol. 39, no. 6, pp. 1129–1138, Jun. 2001.

[44] R. Madhavan *et al.*, "2014 humanitarian robotics and automation technology challenge [humanitarian technology]," *IEEE Robot. Autom. Mag.*, vol. 21, no. 3, pp. 10–16, Sep. 2014.

[45] G. Cabrita, R. Madhavan, and L. Marques, "A framework for remote field robotics competitions," in *Proc. IEEE Int. Conf. Auto. Robot Syst. Comp.*, Apr. 2015, pp. 192–197.

[46] *FP7 TIRAMISU Project—Humanitarian Demining Toolbox*. [Online]. Available: http://www.fp7-tiramisu.eu/, accessed Aug. 6, 2015.

[47] *Clearpath Husky A200, IEEE-RAS Humanitarian Robotics and Automation Technology Challenge (HRATC 2014)*. [Online]. Available: http://www2.isr.uc.pt/~embedded/events/HRATC2014//The_Robot.html, accessed Aug. 6, 2015.

[48] *The Vallon VMP3, Metal Detector Documentation, IEEE-RAS Humanitarian Robotics and Automation Technology Challenge*. [Online]. Available: http://www2.isr.uc.pt/~embedded/events/HRATC2014/bagfiles/documentation/HRATC2014_VallonVMP3.pdf, accessed Aug. 6, 2015.

[49] *Clearpath Husky A200*. [Online]. Available: http://www.clearpathrobotics.com/husky/, accessed Aug. 6, 2015.

[50] *HRATC 2014 Dataset, IEEE-RAS Humanitarian Robotics and Automation Technology Challenge (HRATC 2014)*. [Online]. Available: http://www2.isr.uc.pt/~embedded/events/HRATC2014//Dataset.html, accessed Aug. 6, 2015.

[51] *HRATC 2015 Field Trials, IEEE-RAS Humanitarian Robotics and Automation Technology Challenge (HRATC 2015)*. [Online]. Available: http://www2.isr.uc.pt/~embedded/events/HRATC2015/Field_Trials.html, accessed Aug. 6, 2015.

[52] *The Robot Operating System (ROS)*. [Online]. Available: http://www.ros.org/about-ros/, accessed Aug. 6, 2015.

Davorin Ambruš (M'04) received the Dipl.-Ing. and M.Sc. degrees in electrical engineering from the University of Zagreb, Zagreb, Croatia, in 1999 and 2005, respectively.

He has been with Brodarski Institut Ltd., Zagreb, since 2000, where he has been involved in research, development, project design and management in the area of electronic instrumentation, and sensors and control systems for various industrial applications. In 2012, he joined the Department of Electronic Systems and Information Processing, Faculty of Electrical Engineering and Computing, University of Zagreb, as a Research Associate. His current research interests include computational electromagnetic sensing, electronic instrumentation, and signal processing.

Darko Vasić (S'03–M'10) received the Dipl.-Ing., M.Sc., and Ph.D. degrees from the University of Zagreb, Zagreb, Croatia, in 2002, 2005, and 2010, respectively, all in electrical engineering.

He is currently an Assistant Professor with the Department of Electronic Systems and Information Processing, Faculty of Electrical Engineering and Computing, University of Zagreb. His current research interests include electronic instrumentation and signal processing, specifically, electromagnetic measurement methods, networked sensors, signal detection, and inverse problems.

Vedran Bilas (SM'10) is currently a Professor with the Faculty of Electrical Engineering and Computing, University of Zagreb, Zagreb, Croatia, where he is also the Head of the Laboratory for Intelligent Sensor Systems. He has over 20 years of research, development, and technology transfer experience in the area of sensors and electronic systems. His current research interests include energy-efficient intelligent and networked sensors in various application domains.